# Unraveling the Topological Phase of $ZrTe_5$ via Magnetoinfrared Spectroscopy

Y. Jiang,[1] J. Wang,[2,3] T. Zhao,[2] Z. L. Dun,[2] Q. Huang,[4] X. S. Wu,[3] M. Mourigal,[2] H. D. Zhou,[4] W. Pan,[5] M. Ozerov,[1] D. Smirnov,[1] and Z. Jiang[2,*]

[1]*National High Magnetic Field Laboratory, Tallahassee, Florida 32310, USA*
[2]*School of Physics, Georgia Institute of Technology, Atlanta, Georgia 30332, USA*
[3]*State Key Laboratory for Artificial Microstructure and Mesoscopic Physics, Peking University, Beijing 100871, China*
[4]*Department of Physics and Astronomy, University of Tennessee, Knoxville, Tennessee 37996, USA*
[5]*Quantum and Electronic Materials Department, Sandia National Laboratories, Livermore, California 94551, USA*

(Received 30 March 2020; revised 4 June 2020; accepted 7 July 2020; published 24 July 2020)

For materials near the phase boundary between weak and strong topological insulators (TIs), their band topology depends on the band alignment, with the inverted (normal) band corresponding to the strong (weak) TI phase. Here, taking the anisotropic transition-metal pentatelluride $ZrTe_5$ as an example, we show that the band inversion manifests itself as a second extremum (band gap) in the layer stacking direction, which can be probed experimentally via magnetoinfrared spectroscopy. Specifically, we find that the band anisotropy of $ZrTe_5$ features a slow dispersion in the layer stacking direction, along with an additional set of optical transitions from a band gap next to the Brillouin zone center. Our work identifies $ZrTe_5$ as a strong TI at liquid helium temperature and provides a new perspective in determining band inversion in layered topological materials.

DOI: 10.1103/PhysRevLett.125.046403

Narrow-gap semiconductors and semimetals have regained broad interests in the past decade, as they host a rich variety of topological materials including topological insulators (TIs) and semimetals [1–5]. The low-energy electronic structure of such materials usually exhibits mixing characters of both linear band (LB, $E \propto k$, where $k$ is the wave vector) and parabolic band (PB, $E \propto k^2$), if higher-order terms are neglected. This concept is well reflected in the effective TI model [6,7], which has been proven successful in describing many topological material systems such as HgTe quantum wells [8–10], $Bi_2Se_3$ [6,11], alkali pnictides $A_3Bi$ ($A = $ Na, K, Rb) [12], $Cd_3As_2$ [13], $Pb_{1-x}Sn_xSe$ [14,15], and transition-metal pentatelluride $ZrTe_5$ [16,17].

The rising interest in $ZrTe_5$ is due to the theoretical prediction of a room-temperature quantum spin Hall insulator phase in its monolayer limit [18] and the experimental observation of the chiral magnetic effect [19], anomalous Hall effect [20], and three-dimensional (3D) quantum Hall effect [21] in bulk material. However, because of the delicate dependence of its band topology on the lattice constants [18,22], there has not yet been a consensus on the bulk topological phase of $ZrTe_5$ from experiments [19,23–27], especially with several recent contradicting temperature-dependent studies [28–33]. In these studies, the nontrivial topological phase is either probed through its surface states or relying on the transition behavior of certain indirect parameters such as conductivity. Alternatively, one could also seek to probe the PB component of $ZrTe_5$, which is associated with band inversion and thus provide direct evidence of the band topology without changing external parameters such as temperature and strain. However, this direct approach has not been reported to date.

In this Letter, we show that the LB and PB components of the electronic structure of $ZrTe_5$ can be determined using magnetoinfrared (magneto-IR) spectroscopy, combining Faraday and Voigt geometry measurements. The application of a magnetic field ($B$) quantizes the electronic states into Landau levels (LLs). By carefully tracking the magnetic field dependence of the inter-LL transitions, we can extract important band parameters along the three principal crystal axes and reconstruct the 3D electronic structure of $ZrTe_5$ with great energy resolution. Most saliently, we demonstrate both theoretically and experimentally that the band inversion leads to a second extremum (band gap) next to the Brillouin zone center, giving rise to two distinct sets of inter-LL transitions. Our results unambiguously identify $ZrTe_5$ as a strong topological insulator (STI) at liquid helium temperature.

The $ZrTe_5$ single crystals studied in this Letter were prepared by the Te-assisted chemical vapor transport method [17] or molten Te flux growth [34]. The orthorhombic crystal structure is illustrated in Fig. 1(a). The as-grown samples exhibit a shiny needlelike surface (typically 0.5 by 10 mm) in the $ac$ plane but with a thin thickness (typically 0.1 mm) along the $b$ axis. With such high aspect ratio, the commonly used Faraday geometry measurement, where light travels in the magnetic field direction, is only suitable for studying the electronic structure in the $ac$

 

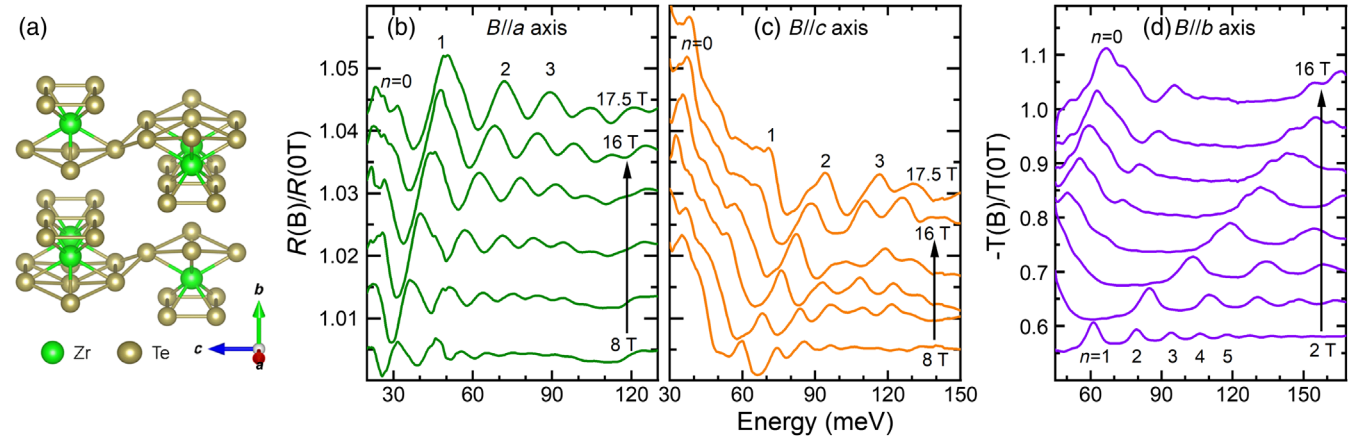


FIG. 1. (a) Schematic view of $ZrTe_5$ unit cell. (b)–(d) Normalized magneto-IR spectra of $ZrTe_5$ with the magnetic field applied along three principal crystal axes. To optimize the signal [35], the spectra with $B\|a$ axis (b) and $B\|c$ axis (c) are measured in Voigt reflection, while those with $B\|b$ axis (d) are measured in Faraday transmission. In (b)–(d), the interband LL transitions $L_{-n(-n-1)} \rightarrow L_{n+1(n)}$ are recognized as spectral peaks and labeled with integer $n = 0, 1, 2, \ldots$. All measurements are performed at liquid helium temperature ($T = 4.2$ K), and the spectra are offset vertically for clarity.

plane, while the Voigt geometry measurement, where light travels perpendicular to $B$, is more effective for the study in the $ab$ and $bc$ planes. Specifically, to optimize the signal, we employed Faraday transmission measurements with $B\|b$ axis and Voigt reflection measurements with $B\|a$ axis and $B\|c$ axis, respectively. All the measurements were performed at 4.2 K with a magnetic field up to 17.5 T. Further crystal synthesis and experimental details can be found in the Supplemental Material [35].

Figures 1(b)–1(d) show the normalized magneto-IR spectra of $ZrTe_5$ with the magnetic field applied along different crystal axes. In all three cases, one can readily identify a series of peaks (or modes), which blueshift as $B$ increases and can be attributed to specific inter-LL transitions $L_{-n(-n-1)} \rightarrow L_{n+1(n)}$ labeled by integer $n = 0, 1, 2, \ldots$. In Figs. 2(a)–2(c), we summarize the magnetic field dependence of the transition energies as a function of $\sqrt{B}$ by extracting the central energy of each mode at different magnetic fields. Here, for simplicity, we focus on the central peak of each transition with the strongest optical weight and omit the weak satellite peaks from the splitting of low-lying transitions.

By comparing the three cases in Figs. 2(a)–2(c), one can see the anisotropy in the electronic structure of $ZrTe_5$. On the one hand, the LL transition energies with $B\|b$ axis [Fig. 2(c)] exhibit a nearly perfect linear-in-$\sqrt{B}$ dependence, characteristic of Dirac-like dispersion. On the other hand, the transition energies with $B\|a$ axis [Fig. 2(a)] and $B\|c$ axis [Fig. 2(b)] grow much more slowly with

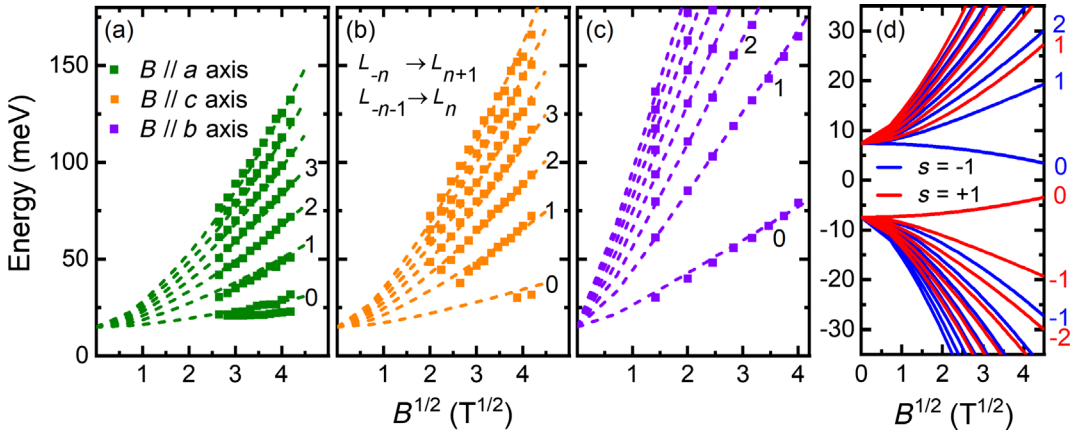


FIG. 2. (a)–(c) Magnetic field dependence of the extracted LL transition energies from Figs. 1(b)–1(d) for $B\|a$ axis (a), $B\|c$ axis (b), and $B\|b$ axis (c), with the symbol size indicating the upper bound of errors in energy positions. The dash lines are best fits to the data using Eq. (2). When splitting occurs, the fit goes through the average energy of the two branches. The interband LL transitions $L_{-n(-n-1)} \rightarrow L_{n+1(n)}$ are labeled by integer $n = 0, 1, 2, \ldots$, consistent with that in Figs. 1(b)–1(d). (d) Representative Landau fan diagram for the case of $B\|a$ axis. The red and blue lines correspond to the $s = \pm 1$ LLs, respectively.

increasing $B$ and show strong deviations from the $\sqrt{B}$ dependence. A closer inspection of Figs. 2(a) and 2(b) also reveals that if one linearly extrapolates (linear in $\sqrt{B}$) the $n \neq 0$ LL transitions to zero magnetic field, a negative energy intercept is obtained. This behavior is very similar to that in inverted PB semiconductors [36,38].

Quantitatively, the modes in Fig. 2(c) can be described by a massive Dirac fermion model [17,37,39], where the LL energies read

$$E_n = \alpha\sqrt{2e\hbar v_F^2 nB + M^2}, \tag{1}$$

with integer $n$ being the LL index, $\alpha = \pm 1$ the band index, $e$ the electron charge, $\hbar$ the reduced Planck's constant, $v_F$ the Fermi velocity, and $M$ the Dirac mass. However, this model fails to explain the data in Figs. 2(a) and 2(b) because (1) the model predicts a positive zero-field intercept regardless of the sign of $M$; (2) for low-lying LL transitions ($n < 3$), the energy ratio of two adjacent modes significantly deviates from the model prediction; and (3) for high-order LL transitions ($n > 3$), the model predicts a linear-in-$\sqrt{B}$ dependence at high magnetic fields but the experimental data curve up. All these deviations from the massive Dirac fermion model suggest strong band anisotropy in $ZrTe_5$ and the necessity to extend the model to include PB contributions.

Next, we show that all our data can be well explained by a $\mathbf{k}\cdot\mathbf{p}$ model that accounts for the symmetry at Γ point, the PB contributions, and the material anisotropy. The effective Hamiltonian [35] reads

$$H(\mathbf{k}) = \begin{pmatrix} L(\mathbf{k}) & 0 & Ak_- & A_z k_z \\ 0 & L(\mathbf{k}) & A_z k_z & -Ak_+ \\ Ak_+ & A_z k_z & -L(\mathbf{k}) & 0 \\ A_z k_z & -Ak_- & 0 & -L(\mathbf{k}) \end{pmatrix},$$

where $L(\mathbf{k}) = M - (\mathcal{B}_x k_x^2 + \mathcal{B}_y k_y^2 + \mathcal{B}_z k_z^2)$, $Ak_\pm = \hbar(v_{Fx}k_x \pm iv_{Fy}k_y)$, and $A_z = \hbar v_{Fz}$. The $x$, $y$, and $z$ directions correspond to the $a$, $c$, and $b$ axes of $ZrTe_5$, respectively. The electronic structure is then determined by a set of material parameters: (1) LB component $\mathbf{v_F} = (v_{Fx}, v_{Fy}, v_{Fz})$; (2) PB component $\mathcal{B} = (\mathcal{B}_x, \mathcal{B}_y, \mathcal{B}_z)$, which is also called the band inversion parameter; and (3) Dirac mass $M$. Both $v_F$ and $\mathcal{B}$ carry anisotropy. The resulting LL spectrum of $ZrTe_5$ reads at $k_z = 0$

$$E_{n=0}^s = s[M - \bar{\mathcal{B}}k_B^2],$$
$$E_{n\neq 0}^s = -s\bar{\mathcal{B}}k_B^2 + \alpha\sqrt{2\hbar^2\bar{v}_F^2 nk_B^2 + (M - M_B)^2}, \tag{2}$$

where $s = \pm 1$, $k_B = \sqrt{eB/\hbar}$ is the inverse magnetic length, and $M_B = 2\bar{\mathcal{B}}nk_B^2$ is the field induced gap. Representative Landau fan diagram for the case of $B\|a$ axis is shown in Fig. 2(d). This model is an extension of the effective TI model [6,7], but due to the band anisotropy, parameters $\bar{\mathcal{B}}$ and $\bar{v}_F$ now represent the geometric average of their values in the plane perpendicular to the magnetic field [35]. That is, for $B\|b$, $\bar{\mathcal{B}} = \sqrt{\mathcal{B}_a\mathcal{B}_c}$, and $\bar{v}_F = \sqrt{v_{Fa}v_{Fc}}$. Note that there is a sign freedom in Eq. (2) since simultaneously reversing the signs of $\bar{\mathcal{B}}$ and $M$ will not affect the results. In this work, we fix the sign of $M$ to be positive and allow the sign of $\bar{\mathcal{B}}$ to vary. A positive (negative) $\bar{\mathcal{B}}$ represents an inverted (normal) band, respectively.

With the above model, one can produce excellent fits to the experimental data in all configurations, as shown in Figs. 2(a)–2(c). Here, we only consider the electric dipole transitions, $\Delta n = \pm 1$ and $\Delta s = 0$, while leaving the discussion of possible $\Delta n = 0$ and $\Delta s = \pm 2$ transitions to the Supplemental Material [35]. Our fitting results of $B\|a$ axis and $B\|c$ axis clearly show that the $M_B$ term breaks the $\sqrt{B}$ energy dependence in Eq. (2) via introducing a linear-in-$B$ mass term (PB contribution). This PB component is comparable with the LB component, suggesting a relatively small $\bar{v}_F$ and/or a relatively large $\bar{\mathcal{B}}$ in these two configurations. When $B\|b$ axis, however, the LB component dominates the LL transition energies due to the large $\bar{v}_F$. In this case, the PB contribution is relatively small, rendering the determination of the $\bar{\mathcal{B}}$ value less accurate in this direction [40]. More importantly, we note that the sign of $\bar{\mathcal{B}}$ cannot be solely determined from the data shown in Figs. 1 and 2, as the most influential PB contribution in Eq. (2), $(M - M_B)^2 \approx M_B^2$ for a small $M$, insensitive to the sign of $\bar{\mathcal{B}}$.

Fortunately, we find an intriguing scenario that can help circumvent the above situation and resolve the topological phase of $ZrTe_5$. This is shown in Figs. 3(a) and 3(b), where we plot the band dispersion along the $b$ axis with different $v_{Fb}$ values for an inverted ($\bar{\mathcal{B}} > 0$) and normal ($\bar{\mathcal{B}} < 0$) band, respectively. For the inverted band [Fig. 3(a)], the electronic structures exhibit a local extremum not only at Γ point but also at a nonzero $k_b$ vector (denoted by $\zeta$ point) when $v_{Fb}$ is sufficiently small. As $v_{Fb}$ increases, the extremum at $\zeta$ point gradually disappears. On the contrary, such extremum at $\zeta$ point never occurs in the normal band case [Fig. 3(b)] regardless of the magnitude of $v_{Fb}$. From our experimental data shown in Figs. 1 and 2, one can extract the $v_F$ values along all three crystal axes with $v_{Fb}$ as small as $\sim 0.5 \times 10^5$ m/s, close to the violet lines in Figs. 3(a) and 3(b). Therefore, the presence of a second extremum at $\zeta$ point signifies band inversion in $ZrTe_5$ and provide a smoking gun evidence for the STI phase. Practically, this direct approach does not require any quantitative analysis, but solid proof of the second extremum.

Since each local extremum in electronic structure carries a large density of states [41], it can host a set of LL

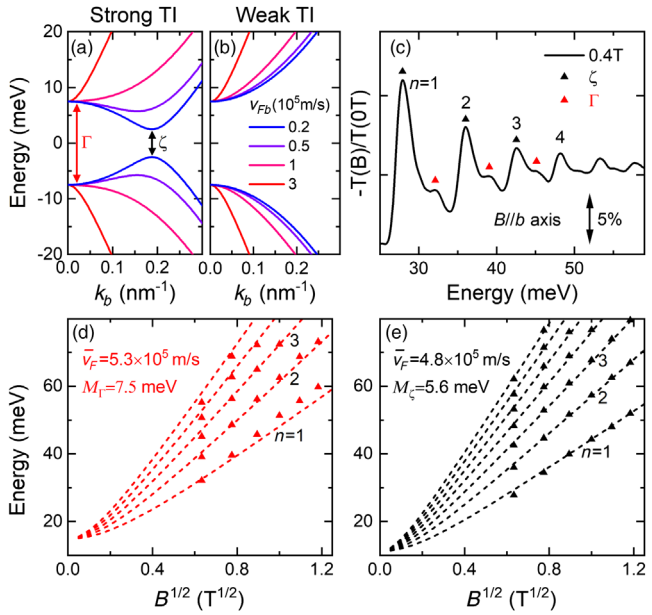


FIG. 3. (a),(b) Zero-field band structures of $ZrTe_5$, calculated in the STI (a) and WTI (b) phases with different $v_{Fb}$. The PB component is kept the same in the calculation but with a positive (negative) sign for the STI (WTI) phase. For STI, two band extrema occur at Γ (red arrow) and ζ (black arrow) points when $v_{Fb}$ is sufficiently small. (c) Normalized magnetotransmission spectrum, $-T(B)/T(0\mathrm{T})$, of $ZrTe_5$ measured at $B = 0.4$ T and $B\|b$ axis. The up triangles label the energy positions of the LL transitions from ζ (black) and Γ (red) points. (d),(e) Best fits to the magnetic field dependence of the LL transitions from Γ (d) and ζ (e) points using the simple massive Dirac fermion model of Eq. (1). The symbol size indicates the upper bound of errors in energy positions.

transitions under a magnetic field. This is indeed the case observed in our experiment when the magnetic field is applied in the slow $v_{Fb}$ direction (when $B\|b$ axis), as shown in Fig. 3(c). Here, due to the high quality of our $ZrTe_5$ samples, clear interband LL transitions ($n = 1, 2, 3, \ldots$) occur in a very low field and unambiguously exhibit a doublet structure (marked by black and red up triangles) before the field-induced linewidth broadening takes place. The energy splitting of the doublet at such a low magnetic field cannot originate from field-induced effects such as $g$-factor or band asymmetry [42]. Linear extrapolation of the magnetic field dependence of the doublet reveals two different energy intercepts at zero field, suggesting that they belong to two distinct sets of LL transitions presumably from the ζ (black) and Γ (red) points, respectively. With increasing $B$, the LB component becomes dominant, and the energy splitting caused by the mass difference between the Γ and ζ points diminishes. Therefore, our results strongly suggest that the $ZrTe_5$ band is inverted, and it is in an STI phase at $T = 4.2$ K.

For more quantitative analysis, one can simply fit each set of the LL transitions with the massive Dirac fermion model of Eq. (1), as a nonzero $k_b$ effectively renormalizes the Dirac mass in our anisotropic model [35]. Figures 3(d) and 3(e) show best fits to the data, where the extracted energy gaps are $\Delta_\Gamma = 2M_\Gamma = 15$ meV and $\Delta_\zeta = 2M_\zeta = 11.2$ meV, respectively. The extracted $\bar{v}_F$ and $M_\zeta$ values in Fig. 3(e) are also consistent with the fitting result of Fig. 2(c). With this information and using the zero-field $\mathbf{k}\cdot\mathbf{p}$ model, one can further deduce $\mathcal{B}_b = 0.21$ eV nm$^2$ [35]. By combining with the fitting results of Figs. 2(a) and 2(b) along the $a$ and $c$ axes, the anisotropy of $\mathcal{B}$ is now fully resolved with improved accuracy. Similarly, the anisotropy of $v_F$ at Γ point can be deduced using the extracted $\bar{v}_F$ values from Figs. 3(d), 2(a), and 2(b).

TABLE I. Extracted band parameters (at Γ point) along the three principal crystal axes of $ZrTe_5$ using the anisotropic $\mathbf{k}\cdot\mathbf{p}$ model.

| $ZrTe_5$ @ Γ point | $k\|a$ | $k\|b$ | $k\|c$ |
|---|---|---|---|
| $v_F$ ($10^5$ m/s) | 6.85 | 0.50 | 4.10 |
| $\mathcal{B}_i$ (eV nm$^2$) | 0.12 | 0.21 | 0.08 |
| $M_i$ (meV) | 7.5 | 7.5 | 7.5 |

In Table I, we summarize the band parameters of $ZrTe_5$ along the three principal crystal axes. Owing to the small $v_{Fb}$, the low-energy electronic structure along the $b$ axis is dominated by the PB component, leading to a much weaker dispersion than those along the LB dominated $a$ and $c$ directions. Our findings are consistent with recent transport and IR experiments [39,43–46].

In conclusion, we have performed a magneto-IR spectroscopy study of the band anisotropy in $ZrTe_5$. We find that the LB dispersion (characterized by $v_F$) along the $b$ axis is about one order of magnitude smaller than those along the $a$ and $c$ axes. When $v_F$ is small, the PB component can strongly modify the band dispersion, and the presence of a second extremum in $b$ direction indicates band inversion. Incorporating prior results of first-principles calculations, we further identify $ZrTe_5$ as an STI at low temperatures. Our work provides an experimental approach to directly infer the topological phase of anisotropic materials from their bulk band structure.

This work was primarily supported by the DOE (Grant No. DE-FG02-07ER46451), while crystal growth at G. T. and U. T. were supported by Grants No. DE-SC0018660 and No. DE-SC0020254. Crystal characterization was performed in part at the GT Institute for Electronics and Nanotechnology, a member of the National Nanotechnology Coordinated Infrastructure, which is supported by the NSF (Grant No. ECCS-1542174). IR measurements were performed at NHMFL, which is supported by the NSF Cooperative Agreement No. DMR-1644779 and the State of Florida. Y. J. acknowledges support from the NHMFL Jack Crow Postdoctoral Fellowship, and Z. J. acknowledges the NHMFL Visiting

Scientist Program. J. W. acknowledges support from the China Scholarship Council. Work at Sandia is supported by a Laboratory Directed Research and Development project and a user project at the Center for Integrated Nanotechnologies, an Office of Science User Facility operated for the DOE Office of Science. Sandia National Laboratories is a multimission laboratory managed and operated by National Technology and Engineering Solutions of Sandia, LLC., a wholly owned subsidiary of Honeywell International, Inc., for the U.S. DOE's National Nuclear Security Administration under Contract No. DE-NA-0003525. This Letter describes objective technical results and analysis. Any subjective views or opinions that might be expressed in the Letter do not necessarily represent the views of the U.S. DOE or the U.S. Government.

*zhigang.jiang@physics.gatech.edu

[1] M. Z. Hasan and C. L. Kane, Rev. Mod. Phys. **82**, 3045 (2010).
[2] X.-L. Qi and S.-C. Zhang, Rev. Mod. Phys. **83**, 1057 (2011).
[3] O. Vafek and A. Vishwanath, Annu. Rev. Condens. Matter Phys. **5**, 83 (2014).
[4] A. A. Burkov, Nat. Mater. **15**, 1145 (2016).
[5] N. P. Armitage, E. J. Mele, and A. Vishwanath, Rev. Mod. Phys. **90**, 015001 (2018).
[6] H. Zhang, C.-X. Liu, X.-L. Qi, X. Dai, Z. Fang, and S.-C. Zhang, Nat. Phys. **5**, 438 (2009).
[7] C.-X. Liu, X.-L. Qi, H. J. Zhang, X. Dai, Z. Fang, and S.-C. Zhang, Phys. Rev. B **82**, 045122 (2010).
[8] M. König, S. Wiedmann, C. Brüne, A. Roth, H. Buhmann, L. W. Molenkamp, X.-L. Qi, and S.-C. Zhang, Science **318**, 766 (2007).
[9] B. Büttner *et al.*, Nat. Phys. **7**, 418 (2011).
[10] J. Ludwig, Yu. B. Vasilyev, N. N. Mikhailov, J. M. Poumirol, Z. Jiang, O. Vafek, and D. Smirnov, Phys. Rev. B **89**, 241406(R) (2014).
[11] M. Orlita, B. A. Piot, G. Martinez, N. K. Sampath Kumar, C. Faugeras *et al.*, Phys. Rev. Lett. **114**, 186401 (2015).
[12] Z. J. Wang, Y. Sun, X. Q. Chen, C. Franchini, G. Xu, H. M. Weng, X. Dai, and Z. Fang, Phys. Rev. B **85**, 195320 (2012).
[13] Z. J. Wang, H. M. Weng, Q. S. Wu, X. Dai, and Z. Fang, Phys. Rev. B **88**, 125427 (2013).
[14] N. Anand, S. Buvaev, A. F. Hebard, D. B. Tanner, Z. G. Chen, Z. Li, K. Choudhary, S. B. Sinnott, G. D. Gu, and C. Martin, Phys. Rev. B **90**, 235143 (2014).
[15] G. Krizman, B. A. Assaf, T. Phuphachong, G. Bauer, G. Springholz, L. A. de Vaulchier, and Y. Guldner, Phys. Rev. B **98**, 245202 (2018).
[16] R. Y. Chen, Z. G. Chen, X.-Y. Song, J. A. Schneeloch, G. D. Gu, F. Wang, and N. L. Wang, Phys. Rev. Lett. **115**, 176404 (2015).
[17] Y. Jiang, Z. L. Dun, H. D. Zhou, Z. Lu, K.-W. Chen, S. Moon, T. Besara, T. M. Siegrist, R. E. Baumbach, D. Smirnov, and Z. Jiang, Phys. Rev. B **96**, 041101(R) (2017).
[18] H. M. Weng, X. Dai, and Z. Fang, Phys. Rev. X **4**, 011002 (2014).
[19] Q. Li, D. E. Kharzeev, C. Zhang, Y. Huang, I. Pletikosić, A. V. Fedorov, R. D. Zhong, J. A. Schneeloch, G. D. Gu, and T. Valla, Nat. Phys. **12**, 550 (2016).
[20] T. Liang *et al.*, Nat. Phys. **14**, 451 (2018).
[21] F. Tang *et al.*, Nature (London) **569**, 537 (2019).
[22] Z. Fan, Q.-F. Liang, Y. B. Chen, S.-H. Yao, and J. Zhou, Sci. Rep. **7**, 45667 (2017).
[23] R. Y. Chen, S. J. Zhang, J. A. Schneeloch, C. Zhang, Q. Li, G. D. Gu, and N. L. Wang, Phys. Rev. B **92**, 075107 (2015).
[24] R. Wu *et al.*, Phys. Rev. X **6**, 021017 (2016).
[25] X.-B. Li, W. K. Huang, Y. Y. Lv, K. W. Zhang, C. L. Yang *et al.*, Phys. Rev. Lett. **116**, 176803 (2016).
[26] G. Manzoni, L. Gragnaniello, G. Autes, T. Kuhn, A. Sterzi *et al.*, Phys. Rev. Lett. **117**, 237601 (2016).
[27] Z.-G. Chen *et al.*, Proc. Natl. Acad. Sci. U.S.A. **114**, 816 (2017).
[28] L. Moreschini, J. C. Johannsen, H. Berger, J. Denlinger, C. Jozwiak, E. Rotenberg, K. S. Kim, A. Bostwick, and M. Grioni, Phys. Rev. B **94**, 081101(R) (2016).
[29] Y. Zhang *et al.*, Nat. Commun. **8**, 15512 (2017).
[30] L. Shen *et al.*, J. Electron Spectrosc. Relat. Phenom. **219**, 45 (2017).
[31] B. Xu, L.-X. Zhao, P. Marsik, E. Sheveleva, F. Lyzwa, Y.-M. Dai, G.-F. Chen, X.-G. Qiu, and C. Bernhard, Phys. Rev. Lett. **121**, 187401 (2018).
[32] J. Mutch, W.-C. Chen, P. Went, T. Qian, I. Z. Wilson, A. Andreev, C.-C. Chen, and J.-H. Chu, Sci. Adv. **5**, eaav9771 (2019).
[33] Y. Tian, N. Ghassemi, and J. H. Ross, Jr., Phys. Rev. B **100**, 165149 (2019).
[34] P. Shahi, D. J. Singh, J. P. Sun, L. X. Zhao, G. F. Chen, Y. Y. Lv, J. Li, J.-Q. Yan, D. G. Mandrus, and J.-G. Cheng, Phys. Rev. X **8**, 021055 (2018).
[35] See the Supplemental Material at http://link.aps.org/supplemental/10.1103/PhysRevLett.125.046403 for crystal synthesis and experimental details, additional experimental data, extended effective Hamiltonian model, and optical weight analysis of magneto-IR spectra, which includes Refs. [36,37].
[36] R. Winkler, *Spin-Orbit Coupling Effects in Two-Dimensional Electron Hole Systems*, Springer Tracts in Modern Physics, Vol. 191 (Springer-Verlag, Berlin, 2003).
[37] M. Orlita, C. Faugeras, R. Grill, A. Wysmolek, W. Strupinski, C. Berger, W. A. de Heer, G. Martinez, and M. Potemski, Phys. Rev. Lett. **107**, 216603 (2011).
[38] For example, see our earlier work: Y. Jiang *et al.*, Phys. Rev. B **95**, 045116 (2017).
[39] E. Martino *et al.*, Phys. Rev. Lett. **122**, 217402 (2019).
[40] Note that the Dirac mass obtained from fitting the data in Fig. 2(c) is slightly smaller than that from Figs. 2(a) and 2(b). This is because the band gap along the $b$ axis is not at $\Gamma$ point, as discussed in the context of Fig. 3.
[41] The $\zeta$ point assigned here is a second extremum of the same band as the $\Gamma$ point. Due to its proximity to the $\Gamma$ point, $\zeta$ point is different from the $Z$ point reported in Refs. [28,29], which belongs to another band across the Fermi energy.
[42] Based on our prior results [17], we estimate the splitting of the $n = 1$ LL transition, due to $g$ factor or band asymmetry,

~0.4 meV, one order of magnitude smaller than the 4 meV splitting observed in Fig. 4(c).
[43] W. Yu, Y. Jiang, J. Yang, Z. L. Dun, H. D. Zhou, Z. Jiang, P. Lu, and W. Pan, Sci. Rep. **6**, 35357 (2016).
[44] X. Yuan *et al.*, NPG Asia Mater. **8**, e325 (2016).
[45] J. L. Zhang, C. Y. Guo, X. D. Zhu, L. Ma, G. L. Zheng, Y. Q. Wang, L. Pi, Y. Chen, H. Q. Yuan, and M. L. Tian, Phys. Rev. Lett. **118**, 206601 (2017).
[46] J. Wang, J. Niu, B. Yan, X. Li, R. Bi, Y. Yao, D. Yu, and X. Wu, Proc. Natl. Acad. Sci. U.S.A. **115**, 9145 (2018).